# Relative Spiral Trajectories for Low-Thrust Formation Flying

By Matthew Willis[1)] and Simone D'Amico[2)]

[1)]*Department of Mechanical Engineering, Stanford University, USA*
[2)]*Department of Aeronautics and Astronautics, Stanford University, USA*

(Received June 21st, 2017)

This work introduces a novel approach to formation flying by extending shape-based continuous thrust trajectory design methods to the relative motion of two spacecraft. The expanding capabilities of high specific impulse electric propulsion systems and multi-satellite formations pose challenges for mission planners which are hereby addressed with a geometrically intuitive, semi-analytical solution to the low-thrust problem. Beginning with the equations of relative motion of two spacecraft, an unperturbed chief and a continuously-thrusting deputy, a thrust profile is constructed which transforms the equations into a form that is solved analytically. The resulting relative trajectories are the family of sinusoidal spirals, which provide diversity for design and optimization based upon a single thrust parameter. Closed-form expressions are derived for the trajectory shape and time-of-flight corresponding to two prescribed relative velocity behaviors. A novel patched-spirals trajectory design and optimization method is developed and applied to the example of a servicer mission to geostationary earth orbit for direct cost comparison of low-thrust and impulsive-thrust architectures.

**Key Words:** Orbital Rendezvous & Proximity Operations, Formation Flying & Satellite Constellations, Trajectory Design & Optimization

**Nomenclature**

Vectors

| | | |
|---|---|---|
| $\mathbf{r}$ | : | Position from central body |
| $\mathbf{u}$ | : | Thrust per unit mass |
| $\mathbf{v}$ | : | Velocity in inertial frame IJK |
| $\boldsymbol{\delta}\mathbf{r}$ | : | Position of deputy from chief |
| $\boldsymbol{\delta}\mathbf{v}$ | : | Relative velocity in rotating RTN frame |
| $\boldsymbol{\delta}\hat{\boldsymbol{\gamma}}$ | : | $\hat{\boldsymbol{\omega}}\times\boldsymbol{\delta}\hat{\mathbf{v}}$ |
| $\boldsymbol{\delta}\hat{\boldsymbol{\theta}}$ | : | $\boldsymbol{\delta}\hat{\mathbf{r}}\times\hat{\boldsymbol{\omega}}$ |
| $\hat{\boldsymbol{\theta}}$ | : | $\hat{\boldsymbol{\omega}}\times\hat{\mathbf{r}}$ |
| $\boldsymbol{\omega}$ | : | Angular velocity of RTN frame in IJK |

Parameters

| | | |
|---|---|---|
| $n$ | : | Chief mean motion |
| $r$ | : | Radial distance to central body |
| $R$ | : | Projection of $\boldsymbol{\delta}\mathbf{r}$ onto $\hat{\mathbf{r}}$ of chief |
| $t$ | : | Time |
| $T$ | : | Projection of $\boldsymbol{\delta}\mathbf{r}$ onto $\hat{\boldsymbol{\theta}}$ of chief |
| $v$ | : | Speed in inertial frame |
| $TOF$ | : | Time of flight |
| $\delta r$ | : | Deputy separation from chief |
| $\delta v$ | : | Deputy speed relative to chief in RTN |
| $\delta\gamma$ | : | Deputy flight path angle in RTN |
| $\delta\theta$ | : | Deputy azimuth from chief radial |
| $\Delta V$ | : | Change in inertial velocity due to thrust |
| $\mu$ | : | Gravity parameter of central body |
| $\xi$ | : | Thrust parameter |

Subscripts and superscripts

| | | |
|---|---|---|
| $0$ | : | Initial |
| c | : | Chief |
| $d$ | : | Deputy |
| $E$ | : | Passive ellipse in RTN frame |
| $f$ | : | Final |
| $IJK$ | : | Derivative in inertial reference frame |
| $RTN$ | : | Derivative in chief's rotating RTN frame |
| $m$ | : | Minimum or maximum |
| $r$ | : | Radial measure of vector |
| $t$ | : | Transverse measure of vector |
| $+$ | : | After patch |
| $-$ | : | Before patch |

## 1. Introduction

The next generation of spacecraft architectures will be characterized by its increased utilization of distributed space systems and low-thrust, electric propulsion systems. To date these concepts have seen limited, but remarkable, service. The successful demonstration of autonomous formation flying in missions such as GRACE,[1)] TanDEM-X,[2)] and PRISMA[3)] has opened the door to advanced mission concepts including distributed occulter/telescopes and on-orbit satellite servicing.[4)] Meanwhile, the development of continuous low-thrust propulsion systems for interplanetary probes such as Deep Space 1[5)] and Dawn[6)] has stimulated the widespread adoption of ion and hall thrusters for satellite station-keeping.[7)] The intersection of these trends creates a problem for mission planners that has received little attention to date: continuous, low-thrust control of spacecraft relative motion. To address the issue, this work adapts and applies shape-based trajectory design methods to the relative motion of two spacecraft.

Missions involving formation flying and rendezvous have historically employed chemical rockets and cold-gas thrusters for maneuvering. For satellite applications, these propulsion systems can produce up to 100 N of thrust and achieve the required maneuver $\Delta V$ over a span of a few seconds.[8)]

Because it is much shorter than the orbital period, this finite timespan may be neglected and the maneuver approximated as impulsive for design purposes. Electric propulsion systems, on the other hand, produce thrusts on the order of 10 μN to 1 N and must operate continuously for a large portion of the orbit to achieve the required $\Delta V$.[9] The tradeoff is that the specific impulse (Isp) realized by electric propulsion systems can range from 1500 to 5000 s, an order of magnitude improvement over the 150 to 300 s attainable with chemical rockets. For this fuel efficiency and their compact nature, electric propulsion systems are particularly valuable to the growing field of micro- and nanosatellites.

The study of low-thrust relative motion began with investigations in optimal rendezvous by Lembeck and Prussing,[10] Carter,[11] and Guelman and Aleshin.[12] Based on the primer vector theory of Lawden,[13] their studies examine rendezvous with unbounded thrust, bounded thrust, and constrained approach direction, respectively. Low-thrust formation control laws based on Lyapunov theory were introduced by de Queiroz et al.[14] and Schaub et al.,[15] based on cartesian and mean orbit element state representations, respectively. These control laws drive the formation toward a prescribed relative trajectory, obtained through a separate treatment of the guidance problem. The NetSat demonstration mission, which consists of a formation of four nanosatellites using electric propulsion, has prompted new research in this area.[16] In particular, Steindorf et al. developed a controller for this formation using a reference governor based on relative orbit elements.[17] In the latter approach, the guidance and control problems are merged into a path-planning problem in the relative orbit elements space. Bevilacqua and Lovell present an analytical approach to spacecraft relative guidance with constant thrust based on relative orbit elements and input shaping, a concept adapted from flexible structure control theory.[18]

Due to the many degrees of freedom introduced by continuous thrust, low-thrust trajectory design is generally formulated as a nonlinear optimization problem. Numerical solvers may be highly sensitive to the search parameters and having a good initial guess is therefore crucial. Shape-based methods provide one route to finding an initial guess, by analytically studying the thrust profile required to follow a prescribed trajectory. The first instance of this method was the study of the logarithmic spiral as a low-thrust, absolute trajectory by Bacon in 1959.[19] Other authors extended the method for the absolute motion of a single spacecraft with more general and useful shapes, such as the exponential sinusoid with variable flight path angle.[20] More recently, Roa showed that the thrust required by the logarithmic spiral trajectory can be extended to a family of generalized logarithmic spirals.[21]

As a first application of shape-based methods to formation flying, this work begins with a development of the equations of relative motion that parallels the classical Hill-Clohessy-Wiltshire (HCW) theory.[22] The dynamics of the relative motion problem differ from those of the absolute motion such that one may treat the trajectory shape and velocity separately. A sinusoidal spiral shape is adopted and two simple strategies for controlling relative velocity are presented.

This paper is organized into three parts. Section 2 presents theoretical developments, starting with the equations of relative motion and derivation of the sinusoidal spirals. Explicit expressions for time of flight are presented for each of the relative velocity control schemes considered. Next, two strategies for patching together relative spiral trajectories are described in section 3. Finally, these strategies are applied to the example problem of a servicer spacecraft visiting a target in geostationary earth orbit (GEO) in section 4.

## 2. Theoretical Development

### 2.1. Equations of Relative Motion

The relative motion of two spacecraft orbiting a central body is governed by the difference of their respective fundamental orbital differential equations as

$$\frac{{}^{IJK}d^2}{dt^2}(\mathbf{r_d}-\mathbf{r_c}) = \frac{\mu}{r_d^3}\mathbf{r_c} - \frac{\mu}{r_c^3}\mathbf{r_d} + \mathbf{u_d} - \mathbf{u_c} \qquad (1)$$

where $\mathbf{r_c}$ and $\mathbf{r_d}$ are the chief and deputy position vectors from the central body, respectively, and $\mathbf{u_c}$ and $\mathbf{u_d}$ are their thrust vectors. The difference in absolute position vectors of chief and deputy in Eq. (1) is equal to the relative position vector $\boldsymbol{\delta}\mathbf{r}$, illustrated in Fig. 1. Making the substitution $\mathbf{r_d} = \mathbf{r_c} + \boldsymbol{\delta}\mathbf{r}$ in the above equation leads to

$$\frac{{}^{IJK}d^2}{dt^2}\boldsymbol{\delta}\mathbf{r} = \mu\left(\frac{\mathbf{r_c}}{r_c^3} - \frac{\mathbf{r_c}+\boldsymbol{\delta}\mathbf{r}}{\|\mathbf{r_c}+\boldsymbol{\delta}\mathbf{r}\|^3}\right) + \mathbf{u_d} - \mathbf{u_c} \qquad (2)$$

The relative velocity in Fig. 1 is defined as the time derivative of the relative position vector $\boldsymbol{\delta}\mathbf{r}$ with respect to the rotating RTN frame of the chief, which may be expressed mathematically as

$$\frac{{}^{RTN}d}{dt}\boldsymbol{\delta}\mathbf{r} \equiv \boldsymbol{\delta}\mathbf{v} \qquad (3)$$

By converting the derivatives in Eq. (2) from *I* to *L* using the angular velocity $\boldsymbol{\omega}$ and applying the definition of relative velocity, the second-order ordinary differential equation (ODE) in Eq. (2) becomes a system of first-order ODEs given by Eq. (3) and

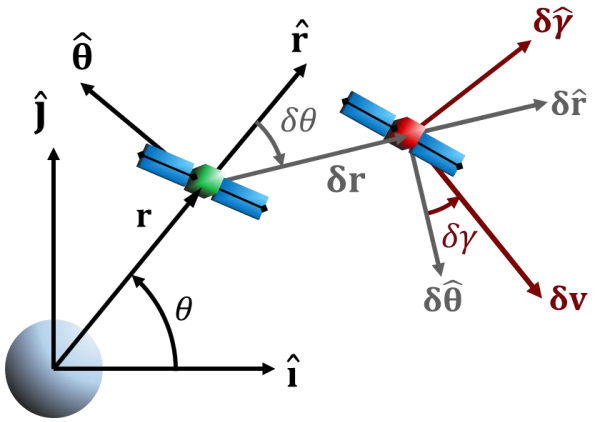


Fig. 1. Geometry of relative motion and definition of polar coordinate systems used to describe the motion of a deputy spacecraft (red) relative to a chief (green).

$$\frac{^{RTN}d}{dt}\boldsymbol{\delta v}+\frac{^{RTN}d\boldsymbol{\omega}}{dt}\times\boldsymbol{\delta r}+2\boldsymbol{\omega}\times\boldsymbol{\delta v}+\boldsymbol{\omega}\times(\boldsymbol{\omega}\times\boldsymbol{\delta r}) = \mu\left(\frac{\mathbf{r_c}}{r_c^3}-\frac{\mathbf{r_c}+\boldsymbol{\delta r}}{\|\mathbf{r_c}+\boldsymbol{\delta r}\|^3}\right)+\mathbf{u_d}-\mathbf{u_c} \quad (4)$$

Equations (3) and (4) provide the most general description of the relative motion of the deputy with respect to the chief, without explicit dependence on the deputy's absolute state or an inertial reference frame. If the chief is in an unperturbed circular orbit, the direction of $\boldsymbol{\omega}$ is constant, its magnitude is $n$, and $\mathbf{u_c}=\mathbf{0}$. After adopting this assumption there is no further need to distinguish between chief and deputy thrusts, so the deputy's thrust will be referred to as $\mathbf{u}$ henceforth.

To convert Eqs. (3) and (4) from vector form to a scalar form suitable for shape-based analysis, the polar coordinate representations of the relative state illustrated in Fig. 1 are introduced. The deputy's relative position is characterized by $\delta r=\|\boldsymbol{\delta r}\|$ and the angle $\delta\theta$, which is measured from $\hat{\mathbf{r}}$ to $\boldsymbol{\delta r}$ with sense opposite to the chief's orbital angular momentum vector. The relative velocity is characterized by $\delta v=\|\boldsymbol{\delta v}\|$ and the relative flight path angle $\delta\gamma$, which is measured from $\boldsymbol{\delta\hat{\theta}}$ to $\boldsymbol{\delta v}$ with sense parallel to the chief's angular velocity vector. To handle motion out of the plane of the chief's orbit, an additional pair of angles or position and velocity measures could be introduced. For the purposes of this discussion, only motion in the chief's orbit plane is considered.

Taking the $\boldsymbol{\delta\hat{r}}$ and $\boldsymbol{\delta\hat{\theta}}$ components of Eq. (3) leads to the scalar differential equations that govern the time-evolution of the relative position variables as

$$\dot{\delta r}=\delta v\sin\delta\gamma \quad (5)$$

$$\dot{\delta\theta}=\frac{\delta v}{\delta r}\cos\delta\gamma \quad (6)$$

Next, taking the $\boldsymbol{\delta\hat{v}}$ and $\boldsymbol{\delta\hat{\gamma}}$ components of Eq. (4), expanding $\|\mathbf{r_c}+\boldsymbol{\delta r}\|^{-3}$ in powers of $\delta r/r_c$, and dropping higher-order terms for small separations leads to the equations

$$\dot{\delta v}=3\,n^2\,\delta r\sin(\delta\gamma-\delta\theta)\cos\delta\theta+\mathbf{u}\cdot\boldsymbol{\delta\hat{v}} \quad (7)$$

$$\delta v\left(\dot{\delta\gamma}-\dot{\delta\theta}\right)=3\,n^2\,\delta r\cos(\delta\gamma-\delta\theta)\cos\delta\theta-2\,n\,\delta v+\mathbf{u}\cdot\boldsymbol{\delta\hat{\gamma}} \quad (8)$$

governing the relative velocity variables. The system of ODEs in Eqs. (5) through (8) is mathematically equivalent to the HCW equations in the chief's orbital plane.

The relative state is often described in terms of a cartesian system centered on the chief, with R, T, and N coordinate axes in the chief's radial, transverse, and out-of-plane directions, respectively. Such a representation is used throughout the discussion to visualize relative trajectories. The $R$ and $T$ coordinates of this system are related to the polar coordinates of Fig. 1 by

$$R=\boldsymbol{\delta r}\cdot\hat{\mathbf{r}}=\delta r\cos\delta\theta \quad (9)$$

$$T=\boldsymbol{\delta r}\cdot\boldsymbol{\hat{\theta}}=-\delta r\sin\delta\theta \quad (10)$$

A similar set of axes can be attached to the deputy and used to describe its inertial velocity in terms of components along basis vectors aligned with the radial and transverse coordinate axes. This representation is useful for describing the deputy's absolute state without explicit dependence on either the state of the chief or an inertially-fixed basis.

### 2.2. Relative Spiral Geometry

By prescribing the deputy's control thrust profile $\mathbf{u}$ in such a way that Eqs. (5) through (8) may be combined to eliminate functional dependencies, one may obtain a closed-form solution for the trajectory in the chief's RTN frame. Due to the choice of state representation, the trajectory shape is controlled by Eq. (8) with explicit dependence only on the $\boldsymbol{\delta\hat{\gamma}}$ component of thrust. The motion of the deputy spacecraft on this trajectory is dictated by Eq. (7) with explicit dependence on the $\boldsymbol{\delta\hat{v}}$ component of thrust.

In principle, a thrust profile could be derived to satisfy any desired trajectory shape. This investigation follows the inverse approach, prescribing a thrust profile that renders the governing equations in solvable form while retaining solution diversity for design and optimization. The thrust profile was chosen to impose a proportionality between $\dot{\delta\gamma}$ and $\dot{\delta\theta}$, controlled by the thrust parameter $\xi$. Examination of Eq. (8) leads to the required thrust profile

$$\mathbf{u}\cdot\boldsymbol{\delta\hat{\gamma}}=\delta v\left[(\xi-1)\frac{\delta v}{\delta r}\cos\delta\gamma+2n\right]-3\,n^2\,\delta r\cos\delta\theta\cos(\delta\gamma-\delta\theta) \quad (11)$$

Equation (11) describes a sliding mode control law, with one part canceling the plant and another imposing the desired dynamics. Because all terms in Eq. (11) scale as $n^2\delta r$, the maximum control thrust with separations smaller than 10 km will vary from mN/kg in LEO to μN/kg in GEO. This thrust range overlaps with that achievable by current electric propulsion systems, so the control law selected is realizable.

Using the thrust profile from Eq. (11) in Eq. (8), one obtains an expression for $\delta\gamma$ in terms of $\delta\theta$ and initial conditions. Combining this relationship with Eqs. (5) and (6) leads to the closed form solution for the trajectory shape

$$\delta r=\begin{cases}\delta r_0\exp[(\delta\theta-\delta\theta_0)\tan\delta\gamma] & \xi=0\\ \dfrac{\delta r_m}{\cos^{1/\xi}[\xi(\delta\theta-\delta\theta_m)]} & \xi\neq 0\end{cases} \quad (12)$$

The geometric parameters $\delta r_m$ and $\delta\theta_m$ have been introduced to eliminate explicit dependence on the initial conditions. These quantities may be obtained from the state variables at any point on the trajectory using

$$\delta r_m=\delta r\cos^{1/\xi}\delta\gamma \quad (13)$$

$$\delta\theta_m=\delta\theta-\frac{\delta\gamma}{\xi} \quad (14)$$

Equation (12) describes the family of sinusoidal spirals, whose diversity is sampled in Fig. 2. For $\xi=0$, the relative flight path angle is constant and the deputy follows either a logarithmic spiral or a circular arc centered on the chief. The trajectory spirals outward if $\delta\gamma>0$ and inward if $\delta\gamma<0$. For $\xi<0$, $\delta\gamma$ decreases as $\delta\theta$ increases, the trajectory solution is bounded, and $\delta r_m$ represents the maximum separation between chief and deputy. For $\xi>0$, $\delta\gamma$ increases with $\delta\theta$, the solution is unbounded, and $\delta r_m$ defines the

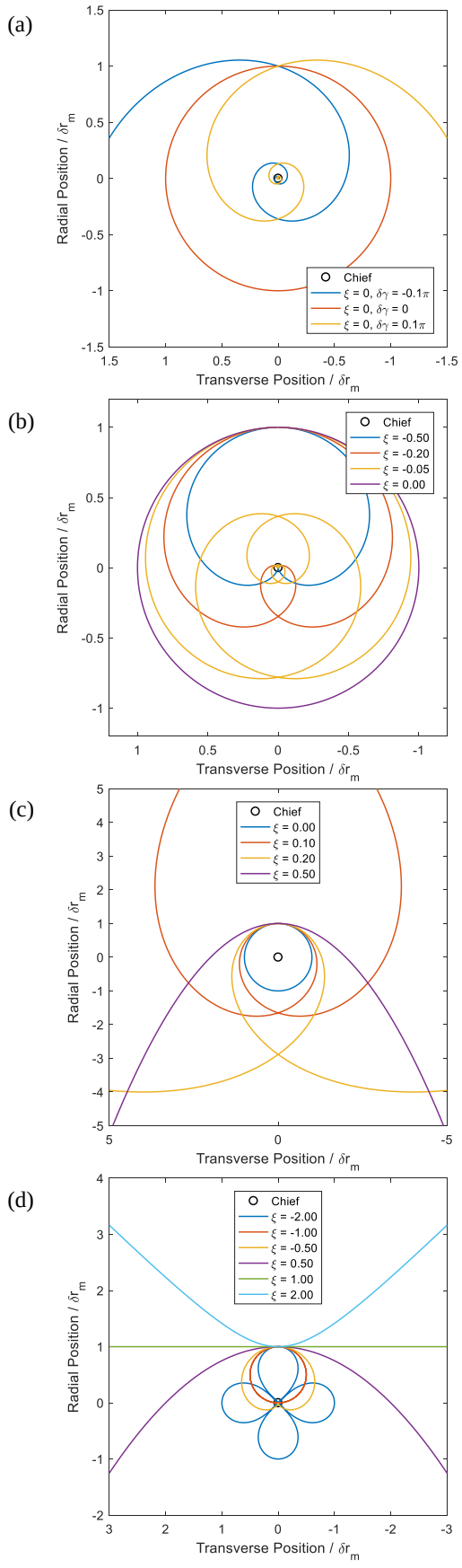


Fig. 2. Geometry of relative spiral trajectory solutions for select values of $\xi$ and $\delta\theta_m = 0$. (a) $\xi = 0$, (b) $-0.5 \le \xi \le 0$, (c) $0 \le \xi \le 0.5$, (d) $\xi \le -0.5$ and $\xi \ge 0.5$.

minimum separation. Note that although the mathematical solution extends to infinity, it is only valid in the region of validity of Eqs. (7) and (8) and the trajectory will be subject to the thrust limitations of the propulsion system. The polar angle $\delta\theta$ is restricted to the range $\delta\theta_m \pm \pi/2|\xi|$, so for $\xi$ between -0.5 and 0.5 the trajectory fully encircles the chief. For $\xi$ outside of this range, the trajectory either converges to the chief or diverges to infinity without crossing itself.

As Fig. 2 illustrates, the family of sinusoidal spirals includes several shapes familiar from classical geometry.[23] These include the logarithmic spiral and circle corresponding to $\xi = 0$ in Fig. 2(a). The spiral with $\xi = -0.5$ in Fig. 2(b) is a cardioid, while that with $\xi = 0.5$ in Fig. 2(c) is a parabola with the chief on the directrix. Fig. 2(d) shows spirals for more extreme values of the thrust parameter, including a straight line for $\xi = 1$, a rectangular hyperbola centered on the chief for $\xi = 2$, a circle passing through the chief for $\xi = -1$, and the Lemniscate of Bernoulli for $\xi = -2$.

### 2.3. Solution Dynamics

Motion along the trajectory is described by $\delta v$ and therefore governed by Eq. (7) with explicit dependence only on the tangential component of thrust. Because this component is orthogonal to the thrust component used to enforce the trajectory shape, it introduces an additional degree of freedom to the analysis. For the current study, two relative velocity control schemes are considered: maintaining a constant ratio of $\delta v$ to $\delta r$ and maintaining a constant $\delta v$. The first is based on the result of linear relative motion theory that the relative speed varies in proportion to the separation, and reduces the extent to which the prescribed thrust must oppose the natural dynamics. The second scheme exercises greater control effort to enable behaviors not achievable by the first. These control schemes were selected for their simplicity and utility, not necessarily for optimality nor to represent the breadth of feasible strategies. Above all, they provide intuition for applying the analytical approach in the discussion to follow.

#### 2.3.1. Constant $\delta v/\delta r$

The requirement for maintaining a constant ratio of $\delta v$ to $\delta r$ is that

$$\frac{d}{dt}\left(\frac{\delta v}{\delta r}\right) = \frac{\delta \dot{v}}{\delta r} - \frac{\delta v}{\delta r^2}\delta\dot{r} = 0 \tag{15}$$

Substitution of Eqs. (5) and (7) into Eq. (15) and applying initial conditions leads to the $\boldsymbol{\delta\hat{v}}$ measure of thrust

$$\mathbf{u}\cdot\boldsymbol{\delta\hat{v}} = \delta v\,\frac{\delta v_0}{\delta r_0}\sin\delta\gamma - 3\,n^2\,\delta r\cos\delta\theta\,\sin(\delta\gamma - \delta\theta) \tag{16}$$

The structure of Eq. (16) parallels that of Eq. (11), with one term to cancel the plant dynamics and another to impose the desired motion. Both terms are comparable in magnitude and whether they add or subtract depends upon the values of $\delta\gamma$ and $\delta\theta$ at a given time.

Thus far, the equations of motion have been solved by replacing time with $\delta\theta$ as the independent variable. However, a sense of time is required for trajectory design. The time of flight is obtained by integration of Eq. (6) using the known dependences of $\delta v$, $\delta r$, and $\delta\gamma$ on $\delta\theta$. This leads to the

analytical expression

$$TOF = \begin{cases} \dfrac{\delta r_0}{\delta v_0}\dfrac{\delta\theta_f - \delta\theta_0}{\cos\delta\gamma_0} & \xi = 0 \\ \dfrac{\delta r_0}{\delta v_0}\left[\ln\delta r + \dfrac{1}{\xi}\ln(\sin\delta\gamma + 1)\right]_0^f & \xi \neq 0 \end{cases} \quad (17)$$

Time of flight takes on a different form based on whether $\delta\gamma$ is constant or variable, i.e. whether $\xi$ is zero or not. In the former case, the deputy's motion about the chief has constant angular velocity and the time of flight is simply the angular separation divided by this constant.

#### 2.3.2. Constant $\delta v$

To maintain a constant relative velocity, the control thrust needs only compensate for the component of the differential gravitational force that is tangential to the curve. From Eq. (7), the resulting thrust profile in the $\boldsymbol{\delta\hat{v}}$ direction is given by

$$\mathbf{u}\cdot\boldsymbol{\delta\hat{v}} = -3\,n^2\,\delta r\cos\delta\theta\sin(\delta\gamma - \delta\theta) \quad (18)$$

and follows the same $n^2\delta r$ scaling as the thrust profiles considered previously.

Again, the dynamics governing $\dot{\delta\theta}$ in Eq. (6) can be directly integrated in terms of the trajectory shape in Eq. (12) and known behavior of $\delta\gamma$ and $\delta v$ to obtain the time of flight. Because $\delta v$ is constant, time of flight is proportional to the path length. This may be understood geometrically for the two $\xi = 0$ cases. For a circular arc, it is the subtended angle divided by the angular velocity. For a logarithmic spiral, it is the change in separation divided by the constant measure of velocity toward or away from the chief. These relationships are expressed mathematically as

$$TOF = \begin{cases} \dfrac{\delta r_0}{\delta v_0}\left(\delta\theta_f - \delta\theta_0\right) & \delta\gamma_0 = 0 \\ \dfrac{\delta r_f - \delta r_0}{\delta v_0\sin\delta\gamma_0} & \delta\gamma_0 \neq 0 \end{cases} \quad (19)$$

For the general case of $\xi \neq 0$, the path length integral is more complicated and time of flight must be expressed in terms of the Gauss hypergeometric function ${}_2F_1(a,b;c;z)$ as

$$TOF = \frac{1}{\xi}\frac{\delta r_m}{\delta v_0}\left[\sin\delta\gamma\ {}_2F_1\left(\frac{1}{2}, 1 + \frac{1}{2\xi}; \frac{3}{2}; \sin^2\delta\gamma\right)\right]_0^f \quad (20)$$

For many special cases, including the classical geometric figures described in section 2.2 above, Eq. (20) reduces to more familiar mathematical functions. A list of such cases is omitted here for brevity but may be found in standard handbooks of mathematical functions such as Abramowitz and Stegun.[24)]

## 3. Patched Spirals

In order to meet demanding mission specifications, multiple sinusoidal spirals can be patched together to form a suitable trajectory. For formation flying missions, it is expected that the patched trajectories share a common reference point. However, it may be desirable to patch together spiral trajectories with reference to different points to add a further degree of freedom to the trajectory design space. These problems are addressed in succession.

### 3.1. Common Reference Orbit

Consider first the scenario of the deputy spacecraft performing low-thrust maneuvers in the vicinity of a chief that is on a circular absolute orbit. In a practical formation-flying mission, the chief might be a cooperative or non-cooperative spacecraft or might represent the geometric center or reference point of a formation. If the separation between chief and deputy has a prescribed upper bound, some portion of the motion must have a thrust parameter $\xi < 0$. Similarly, if the separation has a lower bound, some portion of the motion must have $\xi > 0$. These spirals must be patched together to meet the trajectory requirements. At the patch point, the position and velocity state of the deputy relative to the chief must match, as described by

$$\begin{aligned} \delta r_+ &= \delta r_- \\ \delta\theta_+ &= \delta\theta_- \\ \delta v_+ &= \delta v_- \\ \delta\gamma_+ &= \delta\gamma_- \end{aligned} \quad (21)$$

The conditions in Eq. (21) highlight a fundamental distinction between the methods of patched conics familiar from classical orbital mechanics and the method of patched spirals being described. If the thrust duration is short compared to the orbital period, its effect on the motion can be treated as impulsive for design purposes. Discontinuities in the velocity magnitude and direction result and only the position remains constant across the patch. When continuous low-thrust is used, the short-duration assumption is inherently invalid. Thus, both position and velocity must be continuous at a patch point. Only the thrust may have a discontinuity, but it will not be an impulse.

### 3.2. Distinct Reference Orbits

With the preceding formulation, the range of motion is restricted to the trajectories defined by Eq. (12) over a domain limited by the propulsion system's ability to supply the thrust prescribed by Eqs. (11), (16), and (18). The scope may be dramatically expanded by exploiting the notion that the chief may simply be a reference point and not a physical object, and need not be the same reference point before and after patching. With this introduction of a virtual chief, the relative spiral patching can be applied to relative or absolute orbit control.[25)]

The conditions in Eq. (21) are void without a common reference point, and a new set of patching conditions must be introduced. These follow from continuity of the absolute position and inertial velocity of the deputy across the patch. Expressing the inertial velocity in terms of its radial and transverse measures in the deputy's RTN basis, the new constraints are

$$\begin{aligned} r_{d+} &= r_{d-} \\ \theta_{d+} &= \theta_{d-} \\ v_{dr+} &= v_{dr-} \\ v_{dt+} &= v_{dt-} \end{aligned} \quad (22)$$

These quantities are related to the relative motion variables in vector form by

$$\mathbf{r_d} = \mathbf{r_c} + \boldsymbol{\delta r} \quad (23)$$

$$\mathbf{v_d} = \mathbf{v_c} + \boldsymbol{\delta}\mathbf{v} + \boldsymbol{\omega}\times\boldsymbol{\delta}\mathbf{r} \tag{24}$$

To unpack these equations, take their dot products with the chief's $\hat{\mathbf{r}}$ and $\hat{\boldsymbol{\theta}}$ basis vectors. The resulting scalar conditions are

$$r_d \cos(\theta_c - \theta_d) = r_c + \delta r \cos\delta\theta \tag{25}$$

$$r_d \sin(\theta_c - \theta_d) = \delta r \sin\delta\theta \tag{26}$$

$$\frac{1}{r_d}[v_{dt}\delta r \sin\delta\theta + v_{dr}(r_c + \delta r\cos\delta\theta)] = \delta v \sin(\delta\gamma - \delta\theta) + n\delta r \sin\delta\theta \tag{27}$$

$$\frac{1}{r_d}[v_{dt}(r_c + \delta r\cos\delta\theta) - v_{dr}\delta r \sin\delta\theta] = r_c n - \delta v\cos(\delta\gamma - \delta\theta) + n\delta r\cos\delta\theta \tag{28}$$

where Eqs. (25) and (26) have been used to eliminate $\theta_c$ and $\theta_d$ from Eqs. (27) and (28). Although cumbersome in their present form, Eqs. (27) and (28) are linear in the inertial velocity measures. Solving this system of equations for the inertial velocity measures yields the cleaner relationships

$$v_{dr} r_d = \delta v[r_c \sin(\delta\gamma - \delta\theta) + \delta r \sin\delta\gamma] \tag{29}$$

$$v_{dt} r_d = n r_d^2 - \delta v[r_c\cos(\delta\gamma - \delta\theta) + \delta r\cos\delta\gamma] \tag{30}$$

Equations (25), (26), (29), and (30) constitute the mapping between absolute and relative motion needed to enforce the conditions in Eq. (22) given $r_{c\pm}$ and $\theta_{c\pm}$.

In section 4.1, a virtual chief is introduced to patch relative spirals between initial and final states with known orbit radii and inertial velocity vectors. Rather than matching relative states at a common absolute state, this boundary-value problem requires finding the relative states and common reference point for given initial and final absolute states. The equations required to define the relative spiral in this variant of the problem are now derived.

First, $\theta_d$ and $\theta_c$ may be eliminated from the parameter set by adding the squares of Eqs. (25) and (26) to obtain

$$r_d^2 = r_c^2 + \delta r^2 + 2 r_c \delta r \cos\delta\theta \tag{31}$$

The initial and final relative states, together with $r_c$ then constitute nine unknowns to be determined. Six constraints are provided by Eqs. (29), (30), and (31) at the two boundary conditions. Two additional constraints are provided by the velocity profile and the linear relationship between $\delta\gamma$ and $\delta\theta$. The final constraint is supplied by the trajectory shape from Eq. (12). In terms of the relevant variables, this becomes

$$\frac{\delta r_f}{dr_0} = \begin{cases} \exp[(\delta\theta_f - \delta\theta_0)\tan\delta\gamma] & \xi = 0 \\ \left(\dfrac{\cos\delta\gamma_0}{\cos\delta\gamma_f}\right)^{\frac{1}{\xi}} & \xi \neq 0 \end{cases} \tag{32}$$

This nonlinear system must generally be solved numerically and for given boundary conditions may only have solutions for some range of the thrust parameter $\xi$. However, exact solutions may be obtained for constant relative velocity in the special case of zero radial inertial velocity components at the initial and final states, i.e. patching between apses of the absolute orbit. For most scenarios relevant to relative spiral patching, the radial velocities will be small and these results will provide a good starting point for numerical solution of the full system.

Setting $v_{dr}$ to 0 in Eq. (29) with $\delta v \neq 0$ leads to

$$\delta r = r_c \frac{\sin(\delta\theta - \delta\gamma)}{\sin\delta\gamma} \tag{33}$$

Substituting this expression for $\delta r$ in Eq. (31) and applying trigonometric identities, one finds that

$$\frac{r_d}{r_c} = \pm\frac{\sin\delta\theta}{\sin\delta\gamma} \tag{34}$$

The sign in Eq. (34) is determined by $\text{sign}(r_{di} - r_{dj})$, where $i$ is the state $0$ or $f$ corresponding to $\delta\theta$, $\delta\gamma$, and $r_d$ in the equation, and $j$ is the other boundary state. Substituting $\delta r$ from Eq. (33) and $r_c$ from Eq. (34) into Eq. (30), solving for the constant $\delta v$, and comparing at the initial and final states leads to

$$n = \frac{v_{dt0} + v_{dtf}}{r_{d0} + r_{df}} \tag{35}$$

This remarkably simple expression relates the unknown mean motion of the reference orbit to the deputy's initial and final inertial velocity measures and orbit radii. The altitude of the reference orbit $r_c$ is calculated from $n$ as $\sqrt[3]{\mu/n^2}$. Expressions for $\delta v$ may be found from Eqs. (30) and (35) at either of the boundary states as

$$\delta v = |n r_d - v_{dt}| \tag{36}$$

No restrictions were placed on the relative spiral shape in Eqs. (33) through (36). These equations follow from the choice of constant $\delta v$ control and the relative state variables chosen. At this stage, the relative spiral geometry must be invoked. If $\xi = 0$, $\delta\gamma$ is constant. Dividing Eq. (34) at the final state by itself at the initial state produces a relation between $\delta\theta_0$ and $\delta\theta_f$ as

$$\frac{r_{df}}{r_{d0}} = -\frac{\sin\delta\theta_f}{\sin\delta\theta_0} \tag{37}$$

The variables $\delta\theta_f$, $\delta\gamma$, $\delta r_0$, and $\delta r_f$ can all be related to $\delta\theta_0$ from Eqs. (37), (34), and (33) at the initial and final states, respectively. By inserting these relationships into the $\xi = 0$ trajectory shape expression in Eq. (32), the system is reduced to solving for $\delta\theta_0$ in the single transcendental equation

$$\frac{\delta r_f}{\delta r_0} = \frac{\sin(\delta\theta_f - \delta\gamma)}{\sin(\delta\theta_0 - \delta\gamma)} = \exp[(\delta\theta_f - \delta\theta_0)\tan\delta\gamma] \tag{38}$$

For $\xi \neq 0$, $\delta\gamma$ differs at the initial and final states and cannot be eliminated from Eq. (34) in the derivation of Eq. (37). The system therefore reduces to solving for the unknowns $\delta\theta_0$ and $\delta\theta_f$ in the two transcendental equations

$$\frac{\delta r_f}{\delta r_0} = \frac{\sin(\delta\theta_f - \delta\gamma)}{\sin(\delta\theta_0 - \delta\gamma)}\frac{\sin\delta\gamma_0}{\sin\delta\gamma_f} = \left(\frac{\cos\delta\gamma_0}{\cos\delta\gamma_f}\right)^{\frac{1}{\xi}} \tag{39}$$

$$\delta\gamma_f - \delta\gamma_0 = \xi(\delta\theta_f - \delta\theta_0) \tag{40}$$

where $\delta\gamma_i$ is expressed in terms of $\delta\theta_i$ using Eq. (34).

The exact solution for patching a relative spiral trajectory between a given set of $r_{d0}$, $r_{df}$, $v_{dt0}$, and $v_{dtf}$ with $v_{dr0} = v_{drf} = 0$ is obtained by the following steps. First, $n$ is calculated directly from Eq. (35) and $r_c$ from the definition of $n$, and $\delta v$ from Eq. (36) and $n$. Based on a choice of $\xi$, either Eq. (38) is solved iteratively for $\delta\theta_0$ or Eqs. (39) and (40) are solved simultaneously for $\delta\theta_0$ and $\delta\theta_f$. The remaining parameters are then obtained from Eqs. (37), (34), and (33). If $v_{drf}$ or $v_{dtf}$ is nonzero, this procedure may be used to find an initial guess for numerically solving the full set of constraints in Eqs. (29) through (31) at the initial and final states and Eq. (32).

## 4. Application to GEO Servicer Mission

In this section, a notional satellite servicing mission scenario developed by NASA Goddard is analyzed to demonstrate the utility of the relative spiral trajectories.[26] The mission consists of a servicer spacecraft approaching a noncooperative target in GEO, inserting into a static safety ellipse, and executing a rendezvous with the target to refuel, repair, or boost the target into a disposal orbit.

This scenario provides a practical motivation for the assumptions underlying the relative spiral analytical framework. The high cost of developing and launching GEO satellites makes on-orbit servicing operations to extend lifetimes and remove debris from this region commercially attractive. For a general target satellite, one cannot assume cooperativity or functionality and may only attribute continuous-thrust capabilities to the servicer. The emphasis on circular reference orbits and planar relative motion is well-suited to the GEO belt, whose members lie in coplanar circular orbits. Because of the belt's high altitude, the assumption of small separations is valid and perturbations from atmospheric drag and $J_2$ effects are negligible. Finally, the inherently low mean motion in GEO makes it a prime candidate for continuous-thrust enhancement of the natural dynamics for time-sensitive operations.

Two modifications are made from the reference mission scenario for illustrative purposes. First, the safety ellipse is projected onto the target's orbital plane to accommodate the coplanar framework being considered. In a real mission, the ellipse would be tilted with respect to the target's orbital plane so that the servicer's trajectory does not cross that of the target. The relative motion is then safe in the sense that drift of the ellipse due to a small difference in semi-major axis does not increase the risk of collision. To achieve this relative state, a small out-of-plane velocity component is needed in the final insertion maneuver. This can be accomplished with minor adaptation of the thrust profile, but continuous-thrust control of the out-of-plane motion is saved for future discussion. To distinguish the closed, elliptical relative trajectories subject to natural dynamics from the controlled motions being considered, they will be referred to henceforth as passive ellipses.

The final rendezvous and capture phase of the scenario is replaced with transfer from a larger to a smaller passive ellipse around the target, equivalent to reducing the relative eccentricity vector. Because the constant $\delta v/\delta r$ thrust profile introduced in section 2.3.1 lends itself naturally to continuous-thrust rendezvous from any relative state, this would not add to the discussion of patched spirals. In the modified scenario, the servicer is initially placed in a large passive ellipse around the target to conduct situational awareness observations, then transfers to a second passive ellipse to achieve accurate pose estimation before performing a rendezvous maneuver or departing for a new target.

### 4.1. Formation Establishment

Fig. 3 depicts the approach and passive ellipse insertion phase of the sample mission. The deputy spacecraft, in this case the servicer, is initially placed into a near-circular absolute orbit in the same plane as and approximately 30 km below the target's orbit. This may be accomplished by a launch vehicle upper stage or through a maneuver sequence following a prior mission phase. At the start of the approach scenario, the deputy is 300 km behind the target in the along-track direction. Due to the difference in target and deputy semi-major axes, Keplerian drift reduces the along-track separation over time. Once sufficient angles-only navigation observations have been collected for the navigation filter to converge at this large separation, the deputy maneuvers into a new holding orbit 5 km below the target's orbit. At this higher altitude, the drift is slower and a more accurate state estimate may be obtained before maneuvering into a third holding orbit 1.5 km below the target. The final maneuver establishes the formation by placing the deputy into a passive elliptical relative orbit with a semi-minor axis of 300 m.

The maneuvers in the sequence described above can be divided between two distinct types. One involves the transfer between coplanar circular orbits, with a change only in semi-major axis. The second involves changes in both semi-major axis and eccentricity. In NASA's GEO servicer reference mission scenario, these maneuvers are accomplished with impulsive thrust. The following discussion shows how the analytical techniques developed in section 3.2 may be used to plan these maneuvers with continuous-thrust, relative spiral trajectories.

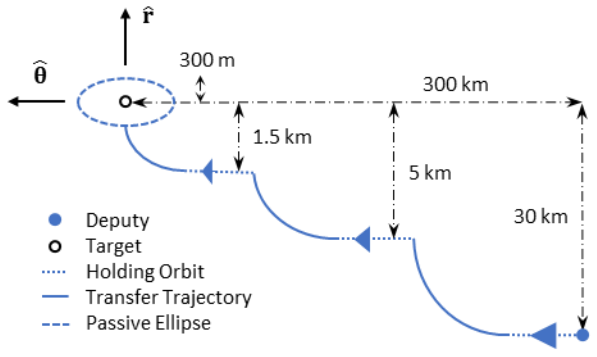


Fig. 3. Formation establishment phase of GEO servicer mission scenario in RTN frame of target, including sequence of orbit-raising maneuvers and insertion into a passive ellipse centered on target. The transfer trajectories shown may represent continuous, low-thrust maneuvers or Keplerian trajectories between impulsive maneuvers (e.g. Hohmann transfers).

To develop insight for this approach, consider first the transfer between two circular orbits. If both chief and deputy are on circular orbits and the deputy is directly below the chief, the relative velocity in the RTN frame is related to their separation by

$$\delta v = \frac{3}{2} n \delta r \tag{41}$$

Because the deputy's orbit is at lower altitude, it advances faster than the chief and the relative velocity is parallel to the chief's velocity vector. The relationship between $\delta r$ and $\delta v$ in Eq. (41) also applies to the case when the deputy is directly above the chief, but the relative velocity is then antiparallel to the chief's velocity vector. This situation is illustrated schematically in Fig. 4. The transfer between concentric circular orbits may therefore be treated as a symmetrical trajectory in the Hill frame of a reference circular orbit midway between the departure and destination orbits. To perform the maneuver using a relative spiral, one may choose the simplest case $\xi = 0$ with $\delta\gamma = 0$, i.e. a circular arc centered on the reference chief (cf. Fig. 2 and Fig. 4). With this choice of thrust parameter, the separation is constant and the same result will be obtained whether the constant $\delta v$ or constant $\delta v/\delta r$ control strategy is adopted.

Although the circular arc is the easiest relative spiral trajectory to understand intuitively, it is not the only solution spiral for this transfer and is not necessarily the best. Effectively, any spiral that sweeps at least $\pi$ radians of $\delta\theta$ before reaching an asymptote can be used to accomplish this maneuver. Due to the rotation of the RTN frame, the simple geometric intuition used to deduce the initial and final states for the $\xi = 0$ case in Fig. 4 cannot be readily applied for $\xi \neq 0$. However, the initial and final flight path angles for this transfer are zero so the simplified form of the constraints in Eqs. (33) through (40) provide the spiral trajectory solutions. Unlike the circular arc, the solution for general $\xi$ will have variable $\delta r$ and the two $\mathbf{u} \cdot \mathbf{d\hat{v}}$ strategies will not produce the same motion.

Solving Eqs. (38) through (40) for a range of $\xi$ values

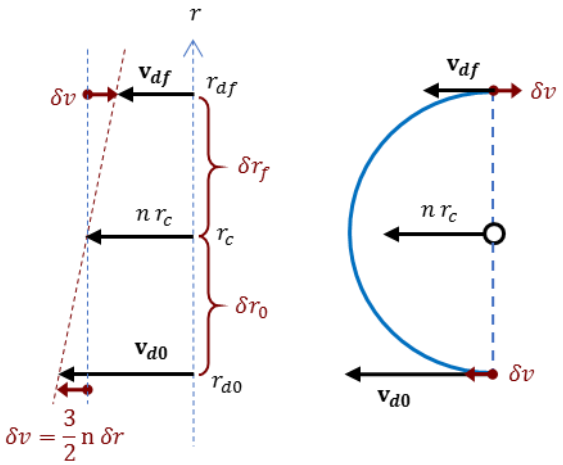


Fig. 4. Geometric development of relative spiral transfer between circular orbits using $\xi = 0$, including relationship between absolute and relative velocity (left) and the shape of the relative spiral transfer in the RTN frame of the virtual chief (right).

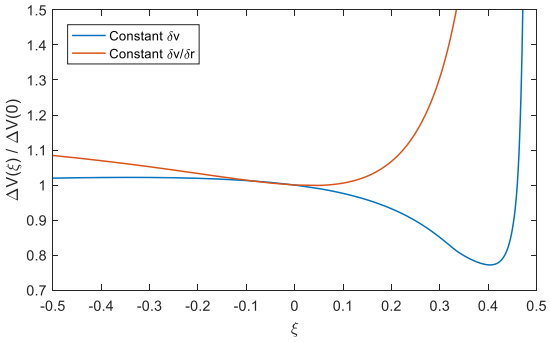


Fig. 5. $\Delta V$-Optimization of transfer with increase in semi-major axis and no change in eccentricity.

allows for optimization over a variety of parameters, as shown in Fig. 5 for $\Delta V$. The vertical axis shows $\Delta V$, computed by integrating the $L_2$-norm of the thrust vector $\mathbf{u}$ for the duration of the transfer, referenced to the value for the $\xi = 0$ case. The correspondence of the $\xi = 0$ case for both control schemes ensures a common scale factor for the vertical axis. This plot was generated for the transfer between circular orbits 30 km and 5 km below GEO, but the shape of the curve is not strongly dependent on the change in altitude so long as $\Delta r_d / r_c < 10^{-3}$.

With the $\mathbf{u} \cdot \mathbf{d\hat{v}}$ profile for constant $\delta v$ from section 2.3.2, a 20% improvement in $\Delta V$ over the $\xi = 0$ case may be achieved using $\xi = 0.41$. This minimum represents a balance between time of flight and trajectory shaping costs. For a single-pass transfer, lower values of $\xi$ demand more control effort to shape the trajectory, but have shorter time-of-flight due to the shorter path-length and constant $\delta v$. Higher values of $\xi$ stretch the relative trajectory in the along-track direction, increasing the flight time and thus the duration of continuous-thrust. With the constant $\delta v/\delta r$ strategy, there is no distinct minimum for $\xi > 0$ because the increase in time of flight is larger than in the constant $\delta v$ case and the longer integration time dominates any shaping advantage. As noted above, the sharp increase in $\Delta V$ as $\xi$ approaches 0.5 is due to the inability of spirals with $\xi > 0.5$ to be tangent to both circular orbits. For values of $\xi$ close to 0 there may be additional solutions which loop around the reference chief multiple times. These multi-pass solutions offer no advantage for the transfers being considered because they increase the flight time.

While Fig. 5 considers optimization only in terms of $\Delta V$, similar plots may be generated for other parameters of interest, such as time-of-flight or maximum thrust in Fig. 6. The discontinuities in slope of the maximum thrust vs. $\xi$ curves are caused by jumps in the location of the thrust peak. Local thrust maxima and minima change in size as the thrust profile varies continuously with $\xi$. For a given set of boundary conditions there will be threshold values of $\xi$ at which one local maximum replaces another as the absolute maximum, resulting in the slope changes observed in the figure. For impulsive maneuvers, $\Delta V$ is the most important cost consideration because of its direct relationship to mass. Due to the high specific impulse of electric propulsion systems, propellant mass considerations may be secondary to flight time and power system constraints which are related to the metrics

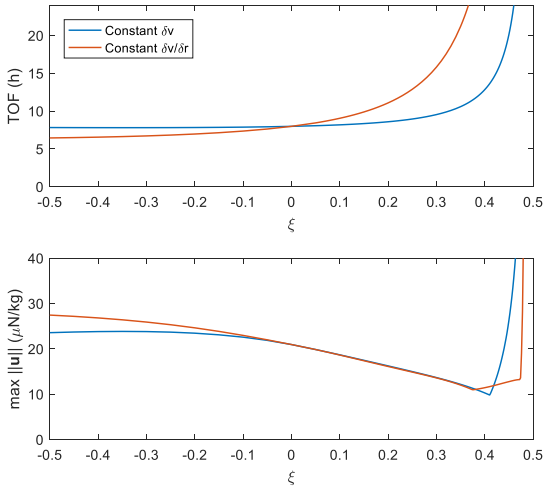


Fig. 6. Optimization of time of flight (top) and maximum thrust magnitude (bottom) for the transfer from a circular orbit 5 km below GEO to another 1.5 km below GEO.

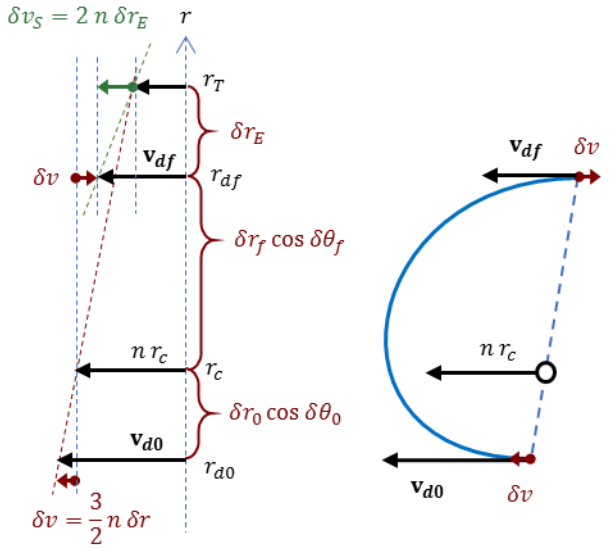


Fig. 7. Geometric development of relative spiral insertion into a passive ellipse with semi-minor axis $\delta r_E$.

of Fig. 6.

The second type of maneuver in the sequence of Fig. 3 involves a change of both semi-major axis and eccentricity. If the semi-major axis of the final absolute orbit matches that of the target, the result is a passive ellipse in the target's RTN frame. For this analysis, the insertion point is assumed to be at perigee of the final orbit, corresponding to the point of the passive ellipse directly below the target. In the linearized relative motion theory, the relative velocity at the positions on a passive ellipse directly above and below the chief is proportional to the separation according to

$$\delta v = 2n\delta r \tag{42}$$

The difference of $1/2\ n\delta r$ between Eqs. (41) and (42) accounts for the excess kinetic energy needed at perigee to reach apogee.

The first step in developing a relative spiral trajectory to accomplish this maneuver is the selection of an appropriate circular reference orbit $r_c$. When transferring between absolute orbits of the same eccentricity, the midpoint could be used as reference because Eq. (41) could be applied to both endpoints. For the transfer involving a change in eccentricity, the velocities at the boundaries relative to a reference orbit at the average altitude will not match. For this fundamentally asymmetric transfer, the reference orbit must be placed below the mean altitude to allow for $\delta v$ windup, as Fig. 7 illustrates. This observation is consistent with the result in Eq. (35). Although the geometry is complicated by the relative dynamics, intuition can be developed by considering values of $|\cos\delta\theta|$ close to one at the boundaries. At the initial condition, the relative velocity is approximated by Eq. (41) with $\delta r \approx \delta r_0$. Similarly, the velocity of the target relative to the reference point at the final condition is approximated by Eq. (41) with $\delta r \approx \delta r_f + \delta r_E$, where $\delta r_E$ is the semi-minor axis of the final passive ellipse. Because the mean motions of the target frame and reference RTN frame are equal to a first approximation, the velocity of the insertion point in the reference RTN frame can be estimated by the difference of the above velocity and the velocity relative to the target in Eq. (42). The initial and final relative velocities are therefore approximated by

$$\begin{aligned} \delta v_0 &\approx \frac{3}{2} n\delta r_0 \\ \delta v_f &\approx \frac{3}{2} n\left(\delta r_f + \delta r_E\right) - 2n\delta r_E = \frac{1}{2} n(3\delta r_f - \delta r_E) \end{aligned} \tag{43}$$

Using the constant $\delta v$ strategy of section 2.3.1, one finds that $\delta r_0 = \delta r_f - \delta r_E/3$ and the reference point must be below the mean transfer altitude. Equation (43) leads to a contradiction if one instead assumes constant $\delta v/\delta r$, so the strategy of section 2.3.2 cannot be used to perform the transfer with change in eccentricity.

Exact solution for this maneuver with $\xi = 0$ and $\xi \neq 0$ can be obtained from the constraints in Eqs. (38) through (40), respectively. The analogue of Fig. 5 for the transfer to a passive ellipse is shown in Fig. 8. The shape of the curve is a strong function of the ratio of $\delta r_E$ to the radial span of the transfer $\Delta r_d$. As $\delta r_E$ approaches zero, the final orbit is circularized and

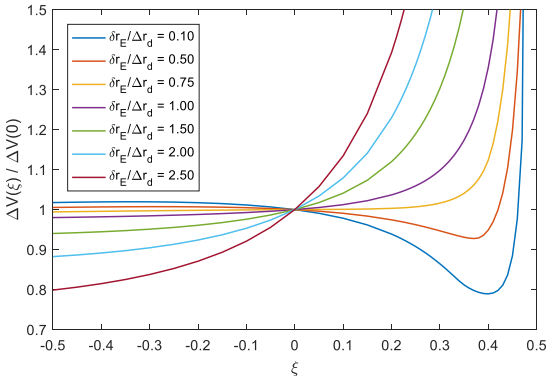


Fig. 8. $\Delta V$-optimization of transfer with change in semi-major axis and eccentricity of $\delta r_E/\Delta r_d$ and constant $\delta v$ control.

the shape of the curve in Fig. 5 is recovered. As the ratio increases, the local minimum moves toward $\xi = 0$ and ultimately vanishes near 0.73. No single-pass transfers of this type are possible for $\delta r_E > 3\Delta r_d$.

The above analyses for the two types of orbit-raising maneuvers may be directly applied to the co-elliptic approach and passive ellipse insertion phases of the example mission scenario. For the prescribed insertion to a passive ellipse with 300 m semi-minor axis from a holding orbit 1.5 km below the target, $\delta r_E/\Delta r_d = 0.25$ and the $\Delta V$-minimizing value of $\xi$ is 0.38. Using this value for the final maneuver and the corresponding value of 0.41 for transfers between holding orbits, one may simulate the maneuver sequence of Fig. 3. The resulting trajectory in the RTN coordinates of the target is shown in Fig. 10, along with the equivalent trajectory accomplished using impulsive Hohmann transfers. This simulation includes the full Keplerian dynamics, but neglects perturbations due to third-body interactions, solar radiation pressure, geopotential, etc., and assumes coplanar motion with both the target and deputy initially on circular orbits. Drift times were distributed evenly across the three holding orbits, leading to a total time of 3.3 days to complete the orbit raising and passive ellipse insertion.

The deputy thrust requirement is shown in Fig. 9, along with propellant consumption assuming nominal Isp values of 300 s and 2000 s for the impulsive- and continuous-thrust scenarios, respectively. Summary results for each maneuver are presented in Table 1. Due in part to kinematic inefficiency, the $\Delta V$ cost for the relative spiral maneuver sequence is higher than for the impulsive transfers. However, the higher specific impulse of electric propulsion systems causes the relative spiral trajectory to have better performance in terms of propellant mass. Because propellant mass effectively limits the number of targets that the deputy spacecraft can visit before retiring or refueling, the continuous-thrust control strategy proposed has a large advantage over the use of impulsive maneuvers.

Two important factors to consider for the continuous-thrust trajectory design are the maximum thrust required and the variation of the thrust level. For electric propulsion systems, the thrust is directly related to the power required, so the maximum thrust will be limited by the spacecraft's power supply.

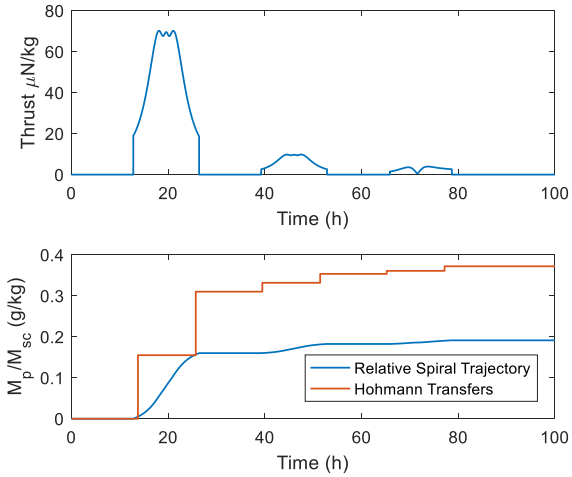


Fig. 9. Deputy thrust profile for relative spiral orbit-raising sequence (top) and comparison of propellant consumption schedules for impulsive and low-thrust trajectories (bottom).

Furthermore, a widely varying thrust profile represents an inefficient use of the power and propulsion systems. Although the thrust magnitudes in Fig. 9 would be feasible for existing electric propulsion systems, the order-of-magnitude difference in peak thrust between maneuvers is undesirable. The discrepancy is caused by the large difference in transfer sizes. Because the thrust profiles in Eqs. (11) and (18) scale as $n^2\delta r$, the 25 km orbit raising maneuver requires seven times the

Table 1. Performance comparison of impulsive- and continuous-thrust maneuver sequences for GEO servicer orbit raising.

| | Impulsive Thrust (Isp 300 s) | | Low-Thrust Relative Spiral (Isp 2000 s) | | |
|---|---|---|---|---|---|
| Maneuver | $\Delta V$ (m/s) | Propellant (mg/kg sc) | $\Delta V$ (m/s) | Propellant (g/kg s/c) | Max Thrust (μN/kg) |
| 25 km raise | 0.912 | 311 | 2.355 | 120 | 70.2 |
| 3.5 km raise | 0.128 | 43 | 0.328 | 16.7 | 9.8 |
| Ellipse insertion | 0.054 | 19 | 0.131 | 6.7 | 3.9 |
| Total | 1.094 | 0.372 | 2.814 | 0.191 | - |

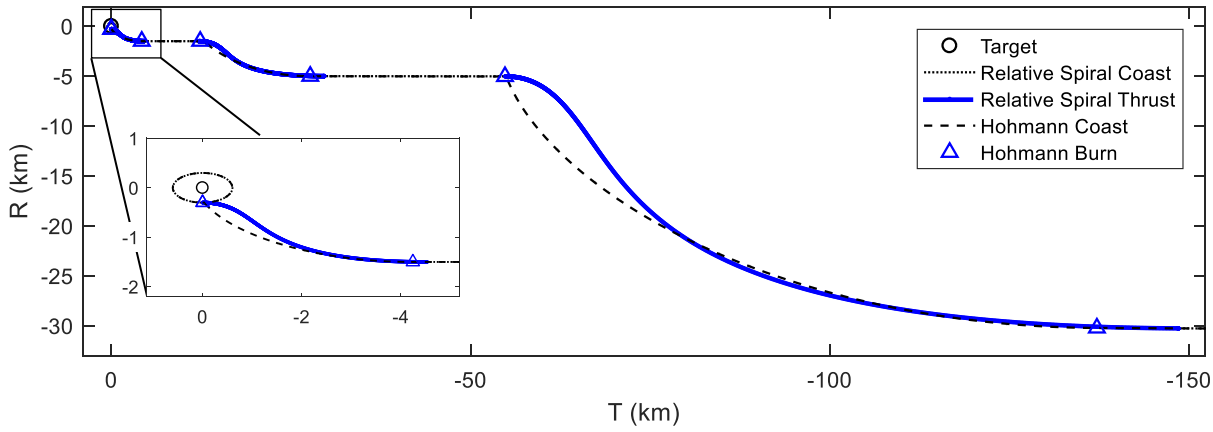


Fig. 10. Comparison of low-thrust relative spiral trajectories with impulsive-thrust Hohmann transfers in RTN coordinates of target for GEO servicer orbit-raising sequence.

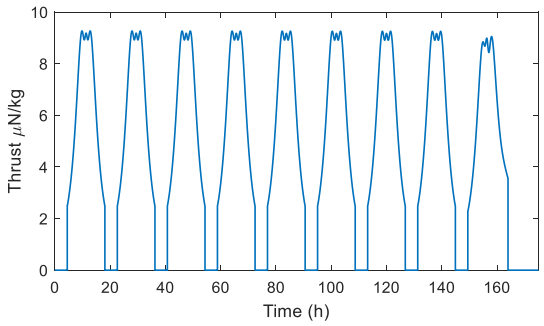


Fig. 11. Thrust profile for relative spiral transfers between equally-spaced holding orbits for GEO servicer orbit raising scenario.

maximum thrust of the subsequent 3.5 km raise. The holding orbits selected were based on a reference scenario developed under the assumption of impulsive maneuvers, but are not critical mission parameters. A relative spiral trajectory with better continuous-thrust performance may be designed by distributing the orbit raising criteria across a greater number of small maneuvers between equally-spaced holding orbits. Fig. 11 shows a thrust profile with nine such maneuvers. The shape of the last thrust curve differs from that in Fig. 9 because the increase in $\Delta r_d$ for the final insertion maneuver shifts the minimizing value of $\xi$ to 0.4 (cf. Fig. 8). Whereas the original scenario required a maximum thrust of 70 μN/kg for the first transfer, each transfer in this updated scenario has a peak thrust requirement of 9.3 μN/kg. The total $\Delta V$ requirement for the sequence remains 2.81 m/s. The tradeoff is that the sequence will now last for a week and the deputy must start more than 750 km behind the chief to accommodate the greater maneuver time and allow for navigation filter convergence on intermediate coasting orbits.

### 4.2. Formation Reconfiguration

After orbiting the target spacecraft long enough on the passive ellipse to collect sufficient situational awareness observations, the servicer spacecraft performs a maneuver to reduce the size of the passive ellipse. This is equivalent to reducing the servicer's orbit eccentricity and thus the relative eccentricity between servicer and target. Because closed, periodic relative motion is desired after the maneuver, the semi-major axis of the servicer's final orbit must match that of the target. Unlike the maneuvers considered in the previous section, the motion in this case is centered around the target and it may be treated as the chief for the analysis. There is no need to introduce artificial reference points and the simpler patching conditions in Eq. (21) apply.

The relative motion on a passive ellipse centered on the chief can be described analytically in terms of $\delta\theta$ and the semi-minor axis $\delta r_E$ as

$$\delta r = \frac{2\delta r_E}{\sqrt{1+3\cos^2\delta\theta}} \tag{44}$$

$$\delta v = n\delta r_E \sqrt{\frac{1+15\cos^2\delta\theta}{1+3\cos^2\delta\theta}} \tag{45}$$

$$\tan\delta\gamma = \frac{3\cos\delta\theta\sin\delta\theta}{1+3\cos^2\delta\theta} \tag{46}$$

Equation (45) is the general form of Eq. (42) and reduces to the latter when $\delta\theta$ is 0 or $\pi$. These equations define the boundary conditions for the formation reconfiguration patched spirals problem. In this example, the initial ellipse has a semi-minor axis of 300 m and the final has a semi-minor axis of 50 m.

For the orbit raising problem considered above, extensive use was made of the control strategy driving constant $\delta v$. That control strategy has limited utility for the new problem of patching spirals between concentric passive ellipses. To understand why, consider the dependence of $\delta v$ on $\delta r$ in Eq. (45). If $\delta v$ is to remain constant throughout the motion and if there can be no discontinuities in $\delta v$ across the patch points, then the $\delta v$ at departure from the first ellipse must equal that at arrival on the second. The square root term in Eq. (45) varies between 2 at $\delta\theta = m\pi$ and 1 at $\delta\theta = (2m+1)\pi/2$ for integer $m$. Two passive ellipses can only contain points with matching $\delta v$ if the size ratio of larger to smaller is less than or equal to 2. The ratio in the present problem is 6, so all points on the inner ellipse have lower $\delta v$ than any point on the outer ellipse and a spiral with constant $\delta v$ cannot satisfy the patching conditions in Eq. (21). Instead, the constant $\delta v/\delta r$ strategy outlined in section 2.3.2 must be adopted.

To facilitate the patched spirals analysis with constant $\delta v/\delta r$, Eq. (45) may be rewritten in terms of $\delta r$ as

$$\delta v = \frac{1}{2} n\delta r\sqrt{1+15\cos^2\delta\theta} \tag{47}$$

Following the same reasoning applied to the constant $\delta v$ case, it is clear that if points on concentric passive ellipses share a common $\delta v/\delta r$, they must also share $\cos^2\delta\theta$. For any departure point on the initial ellipse, there are four compatible locations on the destination ellipse. Two of these are located at $\delta\theta_0 + m\pi$ and have the same relative flight path angle $\delta\gamma$ as the departure point. The other two are at $m\pi - \delta\theta_0$ and have $\delta\gamma$ that is the negative of the departure value.

First consider patching a single relative spiral between two ellipses. The search space can be divided into four regions corresponding to the choice of $\xi = 0$ or $\xi \neq 0$ and $\delta\gamma_f = \delta\gamma_0$ or $\delta\gamma_f = -\delta\gamma_0$. If $\xi = 0$, then $\delta\gamma$ is a constant so any solutions must have $\delta\gamma_f = \delta\gamma_0$. If $\xi \neq 0$, then $|\delta\gamma_f| = |\delta\gamma_0|$ implies that $\delta r_f = \delta r_0$ and the destination ellipse cannot be reached (cf. Eq. (32)). Three of the four regions may thus be eliminated from the outset and only $\xi = 0$, $\delta\gamma_f = \delta\gamma_0$ warrants further examination. The ellipse and relative velocity constraints give $\delta\theta_f = \delta\theta_0 + m\pi$ and $\delta r_f/\delta r_0 = \delta r_{Ef}/\delta r_{E0}$, so Eqs. (32) and (46) become

$$\tan\delta\gamma_0 = \frac{1}{m\pi}\ln\frac{\delta r_{Ef}}{\delta r_{E0}} = \frac{3\cos\delta\theta_0\sin\delta\theta_0}{1+3\cos^2\delta\theta_0} \tag{48}$$

For a given ratio $\delta r_{Ef}/\delta r_{E0}$ and choice of $m$ half-revolutions around the target, Eq. (48) has two solutions in the domain $(0,\pi)$ which are duplicated in $(\pi, 2\pi)$. There can be no solution with $\delta\theta_0 = m\pi/2$ because $\delta\gamma = 0$ and the logarithmic spiral becomes a circle. Fig. 13 shows the two solution trajectories for the specified ellipse ratio and $m = 1$

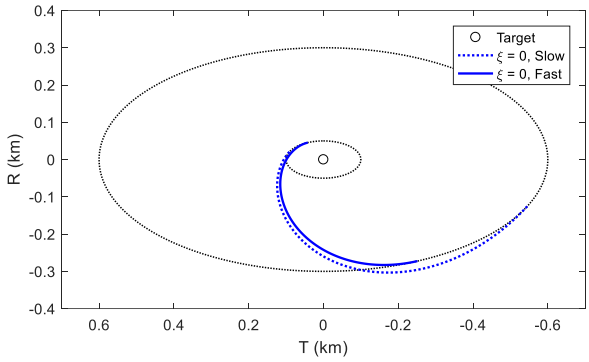


Fig. 13. Half-revolution, single-spiral reconfiguration from a passive ellipse with $\delta r_{E0} = 300$ m to one with $\delta r_{Ef} = 50$ m for a pair of spacecraft in GEO.

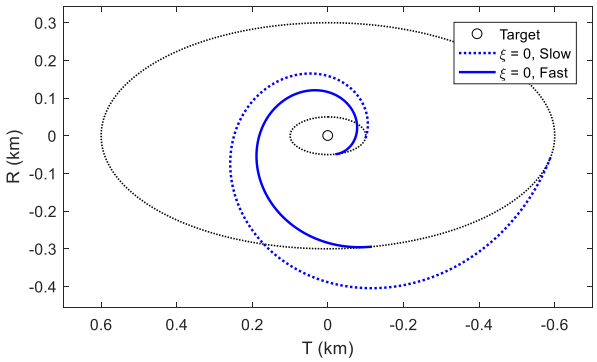


Fig. 12. Full-revolution, single-spiral reconfiguration from a passive ellipse with $\delta r_{E0} = 300$ m to one with $\delta r_{Ef} = 50$ m for a pair of spacecraft in GEO.

in the RTN coordinates of the target. The solutions may be characterized as fast and slow according to their departure point. The trajectory beginning at $\delta\theta_0$ nearer to $\pi/2$ is longer and has lower $\delta v$ than the one beginning nearer to $\pi$. As shown in Fig. 14 and enumerated in Table 2, the fast trajectory takes less time and carries a lower $\Delta V$ cost than the slower trajectory.

In addition to the relative-spiral reconfiguration, Table 2 lists the flight time and cost of the optimal impulsive solution for this reconfiguration.[27] As was the case for orbit raising, the continuous thrust reconfiguration has a higher $\Delta V$ cost than its impulsive counterpart but may be accomplished with less propellant mass. An advantage of the continuous-thrust reconfiguration that was not evident in the orbit raising scenario is the substantial reduction in flight time. Using impulsive maneuvers, the flight time is governed by Keplerian dynamics between maneuvers. For the optimal three-impulse reconfiguration in GEO considered here, a full 24-hour orbital period is required. In contrast, the fast spiral trajectory completes the reconfiguration in just over 9 hours.

The presence of two solutions is a consequence of $\tan\delta\gamma$ assuming all values between -3/4 and 3/4 twice in the domain $(0, \pi)$. If $\delta r_{Ef}/\delta r_{E0} = \exp(\pm 3\pi/4) \approx 0.095$, the two solutions for $m = 1$ merge. For more extreme ratios there are no half-revolution transfers using a single spiral. As $m$ increases or $\delta r_{Ef}/\delta r_{E0}$ increases, the departure point for the fast solution approaches $\delta\theta_0 = \pi$ and the slow approaches $\delta\theta_0 = \pi/2$. This is illustrated for the $m = 2$ case in Fig. 12. Because the slow transfer then departs from a region of lower relative velocity, it experiences an increase in reconfiguration

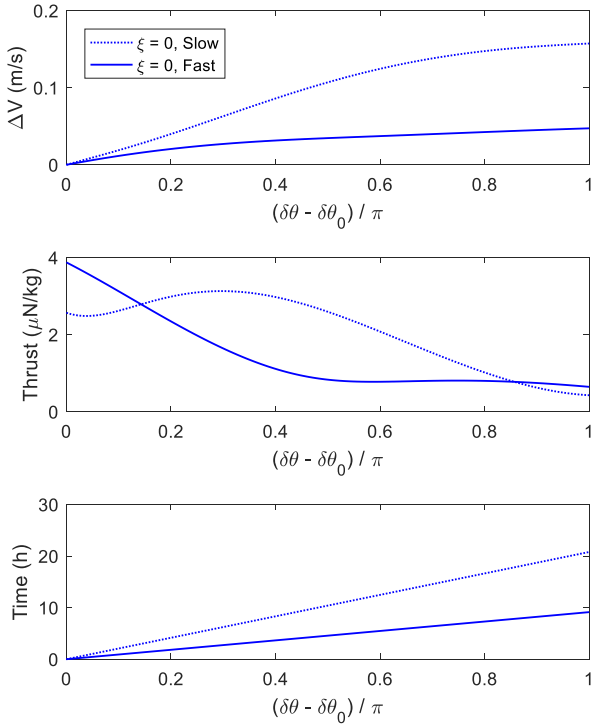


Fig. 14. Comparison of $\Delta V$ cost (top), thrust magnitude (middle), and time-of-flight (bottom) for the fast and slow half-revolution relative spiral reconfiguration maneuvers in Fig. 13.

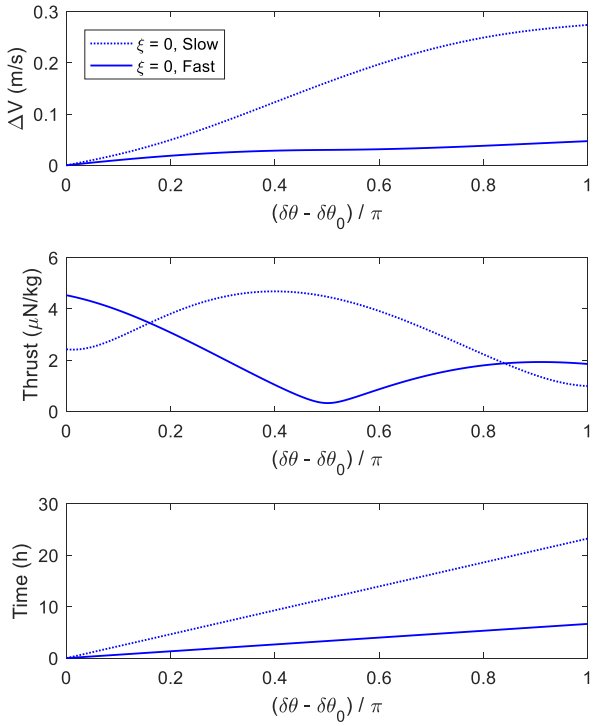


Fig. 15. Comparison of $\Delta V$ cost (top), thrust magnitude (middle), and time-of-flight (bottom) for the fast and slow full-revolution relative spiral reconfiguration maneuvers in Fig. 12.

Table 2. Performance comparison of impulsive- and continuous-thrust maneuver sequences for GEO servicer reconfiguration.

| | Impulsive Thrust (Isp 300 s) | Low-Thrust Relative Spirals (Isp 2000 s) | | | | |
|---|---|---|---|---|---|---|
| | | Single Spiral, $m = 1$ | | Single Spiral, $m = 2$ | | Double Spiral, $m = 1$ |
| | | Fast | Slow | Fast | Slow | |
| $\Delta V$ (cm/s) | 0.91 | 4.73 | 15.73 | 4.72 | 27.4 | 4.04 |
| Propellant (mg/kg sc) | 3.1 | 2.4 | 8.0 | 2.4 | 14.0 | 2.1 |
| Max Thrust (μN/kg) | - | 3.9 | 3.1 | 4.5 | 4.7 | 6.3 |
| Reconfiguration Time (h) | 24.0 | 9.1 | 20.8 | 6.7 | 23.3 | 7.1 |

time and $\Delta V$. The fast transfer, on the other hand, departs from a faster part of the ellipse and experiences a slight decrease in reconfiguration time and $\Delta V$ despite the increase in path length. Because there is a finite limit on the departure $\delta v$, further increasing $m$ leads to longer flight times and higher $\Delta V$ for both the fast and slow trajectories. Consequently, multi-revolution reconfigurations offer little advantage over those shown in Fig. 13 and Fig. 12.

To achieve further improvements in flight time and $\Delta V$, one may increase the number of spirals used in the reconfiguration maneuver. Doing so adds degrees of freedom to the problem, allowing for multiple solutions and optimization. In principle, the number of spirals that may be patched together is arbitrary. For the purpose of providing a flavor for the patching technique, this discussion will be restricted to two spirals. As with the single-spiral case, one may begin by paring down the search space. Due to the restrictions imposed on $\delta\gamma$ and $\delta\theta$ by Eqs. (44) through (46) and the constant $\delta v/\delta r$ control strategy, no sequence involving a logarithmic spiral ($\xi = 0$) can improve upon the single-spiral case. The only case to consider is therefore $\xi_1 \neq \xi_2$ and $\xi_1, \xi_2 \neq 0$. By imposing the patching conditions in Eq. (21) and the geometric relationship in Eq. (32), one obtains the constraint equation

$$\frac{\delta r_{Ef}}{\delta r_{E0}} = \left( \frac{\cos\left(\delta\gamma_0 - m\pi \dfrac{\xi_1\xi_2}{\xi_1 - \xi_2}\right)}{\cos\delta\gamma_0} \right)^{\frac{1}{\xi_2} - \frac{1}{\xi_1}} \tag{49}$$

For a given ellipse size ratio, number of half revolutions, and starting point $\delta\theta_0$, Eq. (49) imposes a relationship between the thrust parameters for the two spirals, $\xi_1$ and $\xi_2$. For half-revolution two-spiral reconfiguration of the ellipses prescribed by the GEO servicer example there is a shallow optimum at $\delta\theta_0 = 0.8\pi$, $\xi_1 = -0.5$, $\xi_2 = -0.08$. The relative trajectory in the RTN coordinates of the target is shown in Fig. 16 and the corresponding $\Delta V$, thrust, and time-of-flight plots in Fig. 17. Numerical results are included with the single-spiral and impulsive reconfiguration results in Table 2. This two-spiral solution achieves a 15% improvement in $\Delta V$ over the fast, half-revolution single-spiral solution while reducing the reconfiguration time by 2 hours.

### 4.3. Inertial Pointing

The preceding section only considers the case of patching between passive ellipses with the natural dynamics of relative motion dictating the boundary conditions. For some applications, the natural dynamics may be unacceptable and continuous-thrust modification of the system may be desirable. For example, the deputy may need to enforce an inertial pointing constraint with the chief or hasten the circumnavigation of a target in a long-period orbit. The relative spiral framework provides a simple tool for designing such trajectories.

As a demonstration, consider a variation on the GEO servicer reconfiguration example. Rather than inserting into a passive

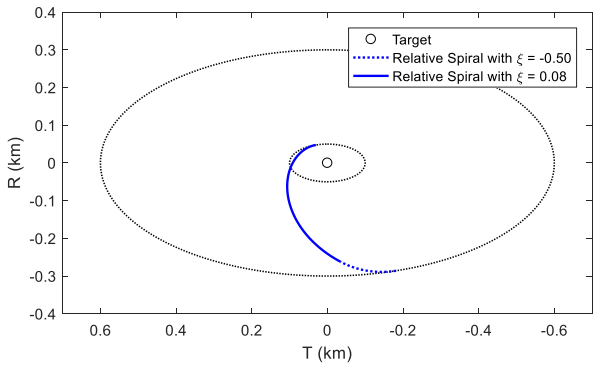


Fig. 16. Optimal half-revolution, two-spiral reconfiguration from a passive ellipse with $\delta r_{E0} = 300$ m to one with $\delta r_{Ef} = 50$ m for a pair of spacecraft in GEO.

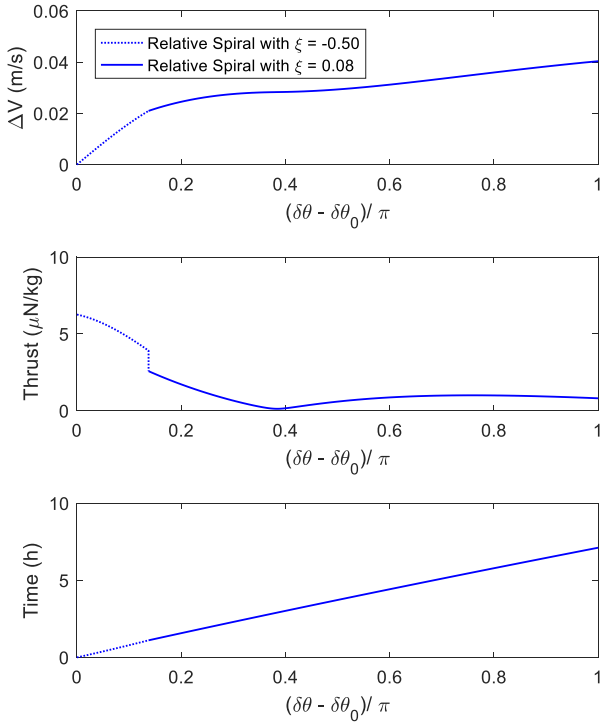


Fig. 17. Comparison of $\Delta V$ cost (top), thrust magnitude (middle), and time-of-flight (bottom) for the optimal half-revolution two-spiral reconfiguration maneuver in Fig. 16.

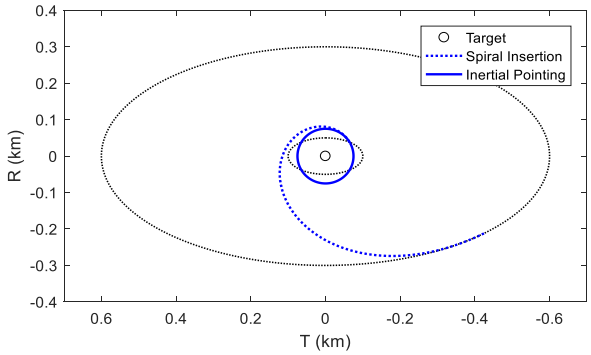


Fig. 18. Single-spiral reconfiguration from a passive ellipse with $\delta r_{E0} = 300$ m to an inertial pointing state with $\delta r_f = 75$ m for a pair of spacecraft in GEO.

spiral around the target, the formation is now required to achieve an inertial pointing state with constant separation equal to the mean separation on the final ellipse considered before.

Constant separation implies that the final state will be a circular relative trajectory and therefore have $\xi = 0$. To maintain inertial pointing on a circular arc, the relative motion must satisfy $\delta v/\delta r = n$. Using the constant $\delta v/\delta r$ control strategy, the relative motion at departure from the initial passive ellipse must also meet this requirement. By inspection of Eq. (47), one may conclude that there are four points on the passive ellipse with $\delta v/\delta r = n$, corresponding to $\cos\delta\theta = \pm 1/\sqrt{5}$. Since $\delta r_f = 1.5\delta r_{Ef} < \delta r_{E0}$, the initial relative flight path angle must be negative and two of these points must be eliminated. The relative spiral used for reconfiguration must have $\delta\gamma = 0$ at the patch point on the circular orbit so $\delta\theta_f = \delta\theta_m$ and $\delta r_f = \delta r_m$. Equations (13) and (46) define the value of $\xi$ for a single-spiral reconfiguration maneuver that satisfies these constraints. The resulting trajectory is shown in Fig. 18 and its time histories in Fig. 19. After an initial $\Delta V$ expenditure of 10.3 cm/s to achieve the inertial pointing configuration, the deputy must expend an additional 5.3 cm/s per revolution for maintenance. If the formation consists of two spacecraft with continuous-thrust capabilities, the cost can be divided equally between them by placing each spacecraft on a circular trajectory of half the size relative to a central reference point.

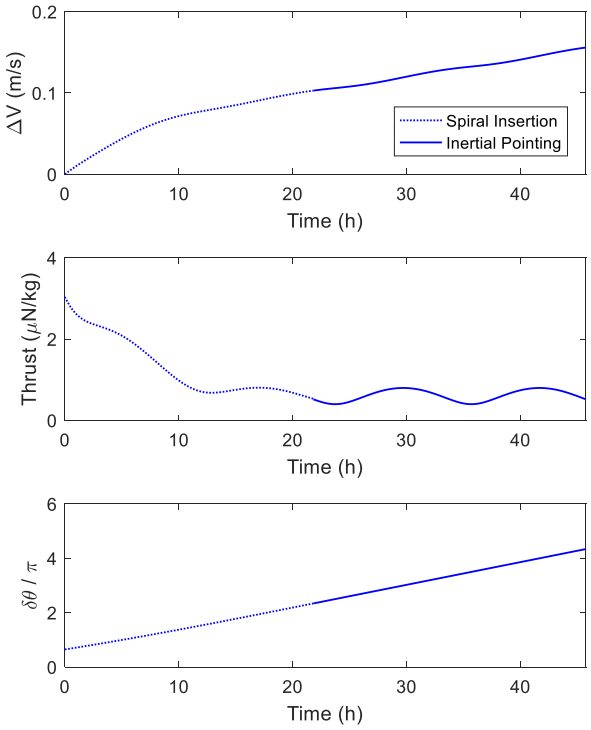


Fig. 19. Comparison of $\Delta V$ cost (top), thrust magnitude (middle), and time-of-flight (bottom) for the single-spiral insertion to and one orbit in an inertial pointing configuration with 75 m separation at GEO.

## 5. Conclusion

This work has introduced the shape-based method of low-thrust trajectory design to the problem of relative motion for two spacecraft. The prescribed thrust profile yields a family of sinusoidal spiral trajectories characterized by the thrust parameter. This family exhibits sufficient variability to generate practical low-thrust trajectories for mission scenarios of interest while providing an analytical handle and geometric insights for design and optimization.

Two approaches were presented for controlling the relative velocity. In one the velocity is kept constant throughout the motion, while in the second the velocity varies in proportion to the separation. Because the thrust magnitude scales as $n^2\delta r$ in each case, the techniques outlined are most practical for MEO and GEO orbits. The example of a servicer spacecraft visiting a target in GEO was used to demonstrate two approaches to patching spiral trajectories and illustrated the utility of the control schemes considered. The constant $\delta v$ strategy has merit for orbit raising in the virtual chief framework, while the constant $\delta v/\delta r$ approach enables reconfiguration of the formation state. When compared to impulsive transfers, both strategies may be used in their respective domains to reduce flight time. This is a large advantage for high altitude orbits in which the natural period may be considerably longer than the timescale of interest.

In its present state, this theory is restricted to coplanar relative motion about a chief in unperturbed circular orbit. However, it may be easily extended to handle out-of-plane motions and elliptical reference orbits. Further efforts should investigate the optimality conditions for maneuver design within the relative spiral framework and develop new relative velocity control schemes accordingly.

## References

1) O. Montenbruck, M. Kirschner, S. D'Amico, S. Bettadpur, "E/I-Vector Separation for Safe Switching of the GRACE Formation," *Aerospace Science and Technology*, Vol 10, No. 7, October 2006, pp. 628-635.

2) J.-S. Ardaens, S. D'Amico, "Spaceborne Autonomous Relative Control System for Dual Satellite Formations," *Journal of Guidance, Control, and Dynamics*, Vol 32, No. 6, November-December 2009, pp. 1859-1870.

3) S. D'Amico, J.-S. Ardaens, R. Larsson, "Spaceborne Autonomous Formation-Flying Experiment on the PRISMA Mission," *Journal of Guidance, Control, and Dynamics*, Vol. 35, No. 3, May-June 2012, pp. 834-850.

4) S. D'Amico, M. Pavone, S. Saraf, A. Alhussien, T. Al-Saud, S. Buchman, R. Bryer, and C. Farhat, "Miniaturized Autonomous Distributed Space Systems for Future Science and Exploration," 8th International Workshop of Spacecraft Formation Flying, Delft University, June 8-10, 2015.
5) J. E. Polk, R. Y. Kakuda, J. R. Anderson, J. R. Brophy, V. K. Rawlin, M. J. Patterson, J. Sovey, and J. Hamley, "Validation of the NSTAR Ion Propulsion System on the Deep Space One Mission: Overview and Initial Results," 35th AIAA/ASME/SAE/ASEE Joint Propulsion Conference, Los Angeles, CA, June 20-24, 1999.
6) C. E. Garner, M. M. Rayman, G. J. Whiffen, J. R. Brophy, S. C. Mikes, "Ion Propulsion: An Enabling Technology for the Dawn Mission." 23rd AAS/AIAA Spaceflight Mechanics Meeting, Kauai, Hawaii, February 10-14, 2013.
7) C. Casaregola, "Electric Propulsion for Station Keeping and Electric Orbit Raising on Eutelsat Platforms," 30th International Symposium on Space Technology and Science, Hyogo-Kobe, Japan, July 4-10, 2015.
8) G. P. Sutton and O. Biblarz, *Rocket Propulsion Elements*. New Jersey: John Wiley & Sons, 2010.
9) D.M. Goebel and I. Katz, *Fundamentals of Electric Propulsion: Ion and Hall Thrusters*. New Jersey: John Wiley & Sons, 2008.
10) C. Lembeck and J. Prussing, "Optimal Impulsive Intercept with Low-Thrust Rendezvous Return," *Journal of Guidance, Control, and Dynamics*, Vol. 16, No. 3, 1993, pp. 426–433.
11) T. E. Carter, "Optimal power-limited rendezvous of a spacecraft with bounded thrust and general linear equations of motion," *Journal of Optimization Theory and Applications*, Vol. 87, No. 3, 1995, pp. 487–515.
12) M. Guelman and M. Aleshin, "Optimal Bounded Low-Thrust Rendezvous with Fixed Terminal Approach Direction," *Journal of Guidance, Control, and Dynamics*, Vol. 24, No. 2, 2001, pp. 378–385.
13) D. F. Lawden, *Optimal Trajectories for Space Navigation*. Butterworths, 1963.
14) M. S. d. Queiroz, V. Kapila, and Q. Yan, "Adaptive Nonlinear Control of Multiple Spacecraft Formation Flying," *Journal of Guidance, Control, and Dynamics*, Vol. 23, No. 3, 2000, pp. 385–390.
15) H. Schaub, S. R. Vadali, J. L. Junkins, and K. T. Alfriend, "Spacecraft Formation Flying Control using Mean Orbit Elements," *AAS Journal of the Astronautical Sciences*, Vol. 48, No. 1, January-March, 2000, pp. 69–87.
16) K. Schilling, P Bangert, S. Busch, et al., "NetSat: a four pico/nano-satellite mission for demonstration of autonomous formation flying," 66th International Astronautical Congress, Jerusalem, Israel, October 12-16, 2015.
17) L. M. Steindorf, S. D'Amico, J. Scharnagl, F. Kempf, and K. Schilling, "Constrained Low-Thrust Satellite Formation-Flying using Relative Orbit Elements," 27th AAS/AIAA Space Flight Mechanics Meeting, San Antonio, Texas, February 5-9, 2017.
18) R. Bevilacqua and T. A. Lovell, "Analytical guidance for spacecraft relative motion under constant thrust using relative orbit elements," AAS 13-471, 23rd AAS/AIAA Space Flight Mechanics Meeting, Kauai, Hawaii, 2013.
19) R. H. Bacon, "Logarithmic Spiral: An Ideal Trajectory for the Interplanetary Vehicle with Engines of Low Sustained Thrust." *American Journal of Physics*, Vol. 27, No. 3, 1959, pp.164–165.
20) A. E. Petropoulos, J. M. Longuski, "Shape-Based Algorithm for the Automated Design of Low-Thrust, Gravity Assist Trajectories." *Journal of Spacecraft and Rockets*, Vol. 41, No. 5, 2004, pp. 787–796.
21) J. Roa, J. Pelaez, and J. Senent, "New Analytic Solution with Continuous Thrust: Generalized Logarithmic Spirals," *Journal of Guidance, Control, and Dynamics*, Vol. 39, No. 10, October 2016, pp. 2336-2351.
22) W. H. Clohessy and R. S. Wiltshire, "Terminal Guidance System for Satellite Rendezvous," *Journal of Guidance, Control, and Dynamics*, Vol 27, No. 9, 1960, pp. 653-658.
23) J. D. Lawrence, *A Catalog of Special Plane Curves*. New York: Dover Publications, 1972.
24) M. Abramowitz and I. A. Stegun, *Handbook of mathematical functions: With formulas, graphs, and mathematical tables.* New York: Dover Publications, 1970.
25) R. E. Sherrill, A. J. Sinclair, T. A. Lovell, K. W. Johnson, and D. D. Decker, "The Virtual-Chief Method for Modeling Relative Motion of Noncircular Satellites," AAS 11-214, presented at the 21st AAS/AIAA Space Flight Mechanics Meeting, New Orleans, Louisiana, 2011.
26) B.W. Barbee, J. R. Carpenter, S. Heatwole et al. "A Guidance and Navigation Strategy for Rendezvous and Proximity Operations with a Noncooperative Spacecraft in Geosynchronous Orbit," *Journal of the Astronautical Sciences*, Vol. 58, No. 3, July 2011, pp.389-408.
27) M. Chernick and S. D'Amico, "New Closed-Form Solutions for Optimal Impulsive Control of Spacecraft Relative Motion," AIAA/AAS Astrodynamics Specialist Conference, AIAA SPACE Forum (AIAA 2016-5659), Long Beach, CA, September 13-16, 2016.